CrossMark

Optical Properties of Cyanoacetylene Ices in the Far- to Near-infrared with Direct Relevance to Titan's Stratospheric Ice Clouds

Melissa S. Ugelow and Carrie M. Anderson
NASA Goddard Space Flight Center, Greenbelt, MD 20771, USA; melissa.ugelow@nasa.gov
Received 2021 August 18; revised 2022 February 28; accepted 2022 March 1; published 2022 April 8

Abstract

Cyanoacetylene (HC_3N) ice has been observed in Titan's stratosphere by both Voyager 1's InfraRed Interferometer Spectrometer (IRIS) and Cassini's Composite InfraRed Spectrometer (CIRS), and it is likely prevalent in other objects in our solar system and exoplanetary systems as well. While previous experimental studies targeting Titan's stratospheric clouds have determined the optical properties of HC_3N ice in the infrared (IR) spectral range, those thin ice films were formed by annealing processes, which contradicts the formation mechanism of Titan's stratospheric ice clouds. As a result, optical constants of HC_3N ices, experimentally created in a similar manner to the way they are formed in Titan's stratosphere, are crucial. Here we experimentally measured absorbance spectra of HC_3N thin ice films from the near- to far-IR spectral region (50–8000 cm^{-1}; 200–1.25 μm) formed via direct vapor deposition at 30, 50, 70, 90, 110, and 113 K. The corresponding optical constants at all temperatures were also computed, resulting in the largest continuous IR spectral range available for HC_3N ice. New tentative peak assignments for spectral features in the near-IR are also reported, thereby further enhancing the inventory of optical constants available for HC_3N ice spanning the near- to far-IR spectral range.

Unified Astronomy Thesaurus concepts: Planetary atmospheres (1244); Atmospheric clouds (2180); Radiative transfer (1335); Titan (2186)

1. Introduction

Cyanoacetylene (HC_3N) is a molecule of great interest due to its prebiotic nature (Ferris et al. 1968; Orgel 2002; Powner et al. 2009; Patel et al. 2015). HC_3N vapor was first detected in interstellar clouds nearly 50 years ago (Turner 1971), and since then, HC_3N vapor has been discovered in protoplanetary disks (Chapillon et al. 2012), comets (Bockelée-Morvan et al. 2000), Titan's stratosphere (Kunde et al. 1981), and possibly even Pluto's atmosphere (Lellouch et al. 2017). In addition to existing as a vapor in Titan's stratosphere, HC_3N also exists in the solid phase, being just one of the many chemical compositions comprising Titan's stratospheric ice clouds observed by Voyager 1's InfraRed Interferometer Spectrometer (IRIS) and Cassini's Composite InfraRed Spectrometer (CIRS; Samuelson 1985, 1992; Khanna et al. 1987; Samuelson et al. 1997; Coustenis et al. 1999; Anderson et al. 2010; Anderson & Samuelson 2011; Anderson et al. 2018a, 2018b; Vinatier et al. 2018). Pure and mixed cyanoacetylene ice has been observed in Titan's stratosphere at northern polar latitudes during northern winter and early northern spring, and pure cyanoacetylene ice has been observed at southern polar latitudes during late southern fall as well (Coustenis et al. 1999; Anderson et al. 2010, 2016, 2018b; Anderson & Samuelson 2011).

In order to interpret ground-based (e.g., Keck), space-based (e.g., James Webb Space Telescope; JWST), or spacecraft-based (e.g., Cassini) observations, optical constants are critically needed to unravel chemical identifications, ice abundances, ice particle sizes, and the radiative impacts of ice clouds. Previous Titan stratospheric-relevant laboratory studies have measured the infrared (IR) spectra of nitrile thin ice films (including HC_3N) and

calculated the corresponding optical constants (see e.g., Masterson & Khanna 1990; Dello Russo & Khanna 1996; Moore et al. 2010). These studies followed an experimental procedure that deposited the nitrile vapors onto a cold substrate at temperatures that resulted in the formation of an amorphous ice. Typically, the amorphous ice was then warmed to its crystalline temperature, which is the coldest temperature at a given pressure where a condensing vapor can still form a purely crystalline ice. The process of warming an amorphous ice is called *annealing*, and it was generally accepted that annealing until the crystalline temperature was achieved would fully convert an amorphous ice into its crystalline phase. After the ice was annealed and its crystalline phase was thought to be achieved, absorption spectra were then collected. Following this, the temperature would be decreased and absorption spectra of the "crystalline" ice would be measured at numerous lower temperatures. The optical constants at the crystalline temperature and at each cooled-down temperature would then be computed. In addition, Moore et al. (2010) collected absorption spectra at numerous temperatures during the ice warm-up, and optical constants of the amorphous ice were computed at those temperatures as well.

While annealing has been the standard experimental method to form a crystalline ice, Moore et al. (2010) discussed that for the nitrile ices they studied, which includes HC_3N, an ice annealed to the crystalline temperature and an ice that formed directly at its crystalline temperature were spectrally different from one another. This includes instances where line widths were broader, peak line centers were shifted in wavenumber, and peak line intensities varied (see Figures 9(a) and 10 in Moore et al. 2010), and these features remained unchanged with longer annealing times. They state that these spectral differences may be a direct result of the structural differences between the ices since they suspect that some of the amorphous fraction of an ice may remain during annealing. As explained further by Anderson et al. (2018a, 2018b) and Nna-Mvondo et al. (2019), despite warming the amorphous

ice to its crystalline temperature, an annealed ice will irreversibly retain some of its amorphous structure. This is further supported by Sandford & Allamandola (1990) who stated that the structure of an ice annealed to the crystalline temperature will be less ordered than when formed directly at the crystalline temperature, which manifests as broader line widths. Due to these inherent structural differences with formation mechanism, the optical properties of an ice annealed to the crystalline temperature will differ from those of an ice formed from direct vapor deposition at its crystalline temperature.

For icy bodies that experience temperature fluctuations, such as cometary comae or ice clouds that form above the stratopause in tenuous atmospheres like that of Pluto (Wong et al. 2017; Gladstone & Young 2019; Lavvas et al. 2020), using the optical constants derived from annealed ices would be preferable to better reproduce the formation conditions of these specific astronomical objects. However, in the case of Titan's stratosphere, trace nitrile and hydrocarbon vapors form at high altitudes in the upper atmosphere (see for example, Yung et al. 1984; Coates et al. 2009; Hörst 2017, and references therein) and are transported downward by atmospheric subsidence to cooler temperatures in the mid to lower stratosphere. It is here in the cooler regions of the mid-to-low stratosphere, with temperatures close to or at the crystalline temperature of many of the nitrile and hydrocarbons present on Titan, that the majority of Titan's trace vapors are abundant enough to condense and form ice clouds via vapor condensation processes (Maguire et al. 1981; Sagan & Thompson 1984; Frere et al. 1990; Samuelson et al. 1997, 2007; Coustenis et al. 1999; Raulin & Owen 2002; Anderson & Samuelson 2011; Anderson et al. 2014, 2016, 2018b). To better reproduce the formation conditions of ice clouds in Titan's stratosphere, whether to interpret remote sensing observations with a radiative transfer model or to simulate the environment with another type of model (e.g., microphysical), it is imperative to incorporate the most accurate optical constants available that best represent the astronomical environment of interest. For the case of Titan's stratosphere, optical constants derived from direct vapor deposition experiments at temperatures corresponding to the observed cloud formation altitudes are essential, and do not exist for HC_3N. Also, performing these studies on pure ices will help unravel the chemical identity and complexity of Titan's stratospheric clouds, namely if they are composed of pure ices or of co-condensed ices. Even more so, to fully understand the characteristics of a co-condensed ice, the characteristics of the pure ices must be known first.

Here, using the SPECtroscopy of Titan-Related ice Analogs (SPECTRAL) chamber (see Anderson et al. 2018a, for a detailed experimental setup), we performed transmission spectroscopy on HC_3N ices formed via direct vapor deposition at temperatures between 30 and 113 K. This is the first study of its kind to measure the transmission spectra of HC_3N ice across the large spectral range of 50 to 8000 cm^{-1} (200 to 1.25 μm), and report on their optical constants over this entire spectral range for each deposition temperature.

2. Experimental Methods

2.1. HC₃N Synthesis

Cyanoacetylene was synthesized following the procedures described in Moureu & Bongrand (1920), Miller & Lemmon (1967),

and Graupner et al. (2006), with certain modifications that are described in the following paragraph. Propiolamide (Alfa Aesar, 96%), phosphorus pentoxide (Sigma Aldrich, 98.6%), and dried sand were combined in a 1:4:4 ratio by mass in a dry, argon-purged glove box (relative humidity $\leqslant$ 19%). In a round-bottom flask attached to a glass manifold under a medium vacuum (3 × 10^{-3} mbar), the reactants were slowly heated from 25 to 160°C, at a rate of 1°C min^{-1}.

Numerous steps were taken to minimize contamination from atmospheric H_2O, reaction by-products including CO_2, and HC_3N polymerization. To reduce contaminants, product was only collected in a sample vial once the reaction reached 95°C. Pumping on the reacting mixture until this temperature was met resulted in a noticeable decline and removal of certain contaminants, observed via IR spectroscopy as a reduction in the strength of the contaminant spectral features. Moreover, to inhibit CO_2 contamination, after the reaction reached 95°C, the product was immediately collected in a liquid N_2–ethanol slush bath (−116°C) as the reaction mixture continued to be heated. This allowed CO_2 to remain in the gas phase for easy removal. Following the synthesis, the ice was further purified of CO_2 and H_2O by performing purification cycles similar to the freeze-pump-thaw method; however, the ice was never allowed to thaw. Purification was accomplished utilizing two slush baths at two different temperatures, alternating between each slush bath while constantly pumping on the ice. The first slush bath contained the initial liquid N_2–ethanol mixture at −116°C and the second consisted of a liquid N_2–acetone mixture held at −94°C. And lastly, keeping cyanoacetylene frozen upon its formation and during its purification was essential to limit the extent of polymerization, given that cyanoacetylene readily polymerizes as it approaches room temperature.

It is essential that contaminants are removed from the sample prior to vapor deposition since their presence typically results in the spectral shifting of the pure ice features (see for example, Anderson et al. 2018a). While it may be thought possible to simply remove the spectral features corresponding to the contaminants in the absorbance spectra during the post-processing phase, this approach is not equivalent to purifying the sample prior to vapor deposition. The most commonly used optical constants available for HC_3N ice in the IR are from Moore et al. (2010), and these data suffer significantly from CO_2 contamination, reinforcing the need for HC_3N optical constants over this spectral range that are free from CO_2 contamination.

2.2. Experimental Procedure and Data Processing

A detailed description of the SPECtroscopy of Titan-Related ice Analogs (SPECTRAL) ice chamber, combined with our standard vapor deposition method and post-processing procedures, is given in Anderson et al. (2018a). To summarize, thin ice film transmission spectroscopy from 50 to 8000 cm^{-1} (200 to 1.25 μm) was performed using a Fourier Transform IRspectrometer (Nicolet, model iS50R) in the SPECTRAL chamber. The far-IR configuration utilizes a solid-state beamsplitter and a DTGS detector with a polyethylene window, while the mid-IR configuration employs a KBr beamsplitter and a Mercury Cadmium Telluride (MCT)-A detector with a CdTe window. For the far- and mid-IR experiments, averaged spectra of 2048 and 256 scans, respectively, were recorded at a spectral resolution ($\Delta\nu$) of 2.75 cm^{-1}, then background-corrected and averaged to produce a raw absorbance spectrum

with 1.38 cm^{-1} spacing. The error in line position is a function of the line width, the signal-to-noise ratio, and the spectrometer's accuracy in wavenumber position (0.01 cm^{-1}), and was calculated for the lattice and fundamental modes following the procedure described in Condon (1997). See Table 1 for specific line center accuracies for these HC$_3$N ice spectral features.

Since HC$_3$N quickly polymerizes at room temperature, adaptations to our standard deposition method were made. First, the glass vial containing frozen HC$_3$N was attached to the inlet of the SPECTRAL chamber while submerged in a liquid nitrogen–filled dewar. Then, upon removing the dewar, the ice sublimed in the presence of helium gas (in at least a 25:1 ratio with HC$_3$N vapor). By including a large mixing ratio of helium gas in the lines when depositing HC$_3$N, the likelihood of polymerization was significantly decreased and gaseous HC$_3$N was stabilized. This is demonstrated in Figure 1, which shows two HC$_3$N depositions at 30 K, one with helium gas and one without helium gas. In the absence of helium, there are two confirmed spectral features due to polymer that emerge, one near ~1640 cm^{-1} (panel b) and the second feature is the broad doublet at 3545 and 3625 cm^{-1} (panel d). However, the presence of helium greatly reduced these polymer spectral features to below the spectrometer's detection limit, with no impact on the spectral dependence of HC$_3$N ice (see Figure 1 panels a–d).

Next, the mixed HC$_3$N and helium vapors were flowed into the vacuum chamber using a variable leak valve. HC$_3$N vapor condensed onto a cold chemical vapor deposition diamond substrate, located at the center of the high vacuum spherical sample chamber (10^{-8} Torr), while the helium was removed by vacuum pumping. We typically deposit vapors at a rate between 0.1 and 0.5 μm min^{-1} (see Anderson et al. 2018a); however, in order to reduce the time HC$_3$N spent in the gas phase, the rate of our HC$_3$N deposits were in the middle of this range, averaging ~0.3 μm min^{-1}.

As described in Anderson et al. (2018a), the growth of the ice film was monitored as a function of vapor deposition time via double laser interferometry using two 5 mW laser diodes (532 nm and 635 nm). Then, using the Bragg equation (see e.g., Tempelmeyer & Mills 1968; Domingo et al. 2007) and the refractive index n$_0$ for amorphous and crystalline HC$_3$N from Moore et al. (2010), the thickness of the ice d was computed. The 1σ uncertainty in d was then calculated through standard error propagation using the uncertainty in n$_0$ determined by the medium absolute deviation. At each temperature studied, the HC$_3$N ice film thicknesses ranged between 0.75 and 0.82 μm (with up to 2.67% uncertainty), which we targeted to avoid saturating the ν_1 band of HC$_3$N (in the mid-IR). Since the far-IR detector is less sensitive than the mid-IR detector, the lattice and ν_7 spectral features were reduced in strength at this film thickness. Even so, this was necessary to ensure the far- and mid-IR spectra remained internally consistent in thickness when creating the composite spectrum during post-processing, necessary to compute the optical constants across the continuous 50–8000 cm^{-1} spectral range.

The HC$_3$N experiments were first performed at 30 K to check for sample purity (CO$_2$, H$_2$O, polymers, etc.). Once the ice was confirmed to be pure (i.e., contaminants were below the spectrometer's detection limit), warmer vapor deposition temperature experiments were performed at 50, 70, 90, 110, and 113 K. Between experiments, the glass vial with the remaining HC$_3$N was stored in a −85°C freezer. During the post-processing phase, the IR channel fringes contained in the raw absorbance spectra were removed and then an iterative Kramers–Kronig analysis technique was applied to calculate the optical constants. For a detailed explanation on the ice thickness calculation, channel fringe removal, and the program used to calculate the optical constants, see Anderson et al. (2018a).

3. Results and Discussion

Figure 2 shows the full spectral range measured for amorphous and crystalline HC$_3$N ice formed by direct vapor deposition at 30 and 113 K, respectively, and their corresponding optical constants. The absorbance features and the imaginary part of the refractive index (k) values at wavenumbers greater than 3800 cm^{-1} (wavelengths shorter than 2.63 μm) have been multiplied by 50 to aid in viewing these numerous but weak combination and overtone bands. Absorbance spectra were also taken at direct deposition temperatures of 50, 70, 90, and 110 K, and their optical constants were calculated as well. While previous studies reported absorbance spectra and optical constants that covered portions of our spectral range (Masterson & Khanna 1990; Dello Russo & Khanna 1996; de Bergh et al. 2008; Moore et al. 2010), the 50–8000 cm^{-1} spectral range measured in this current study is the largest known spectral range in the IR for HC$_3$N ice formed at numerous vapor deposition temperatures. Therefore, this is the first study to report on the absorbance spectra and complex refractive indices of HC$_3$N directly deposited at 30, 50, 70, 90, 110, and 113 K over this large spectral range. In addition, to the best of our knowledge, the optical constants calculated by de Bergh et al. (2008) in the near-IR are not available in a tabulated format, and would need to be digitized from their figure. Therefore, the optical constants reported here are the only known publicly available source for HC$_3$N ice at wavenumbers greater than 5000 cm^{-1} (wavelengths shorter than 2 μm).

In order to discern the HC$_3$N fundamental vibrational mode spectral features more clearly, Figure 3 includes the channel fringe corrected spectra from 50–550 cm^{-1} (left; 200–18.2 μm), 625–1600 cm^{-1} (middle; 16–6.25 μm), and 2000–3400 cm^{-1} (right; 5–2.94 μm). Figure 4 also includes the channel fringe corrected spectra of the weaker overtone and combination bands in the near-IR, spanning 3800–8000 cm^{-1} (2.63–1.25 μm). Table 1 includes the assignment for each HC$_3$N feature, along with labeling of known features that do not correspond to HC$_3$N ice. For example, features with footnote "a" in the assignment column are those that noticeably decreased in intensity when HC$_3$N was deposited with helium gas, and are therefore likely related to polymer. For HC$_3$N, the lattice mode and ν_7 are somewhat noisy (due to the thickness of the ice), and the assigned wavenumber positions were determined based on the peaks that were above the noise. In addition, features with a question mark next to their assignment are those that have either never been observed or assigned in the literature. This includes numerous features at wavenumbers greater than 4000 cm^{-1} (wavelengths shorter than 2.5 μm), which are HC$_3$N combination bands and overtones that have been observed by Quirico et al. (1999), but were never assigned. Producing never-before-published optical constants and absorbance spectra at higher wavenumbers (shorter wavelengths) into the near-IR will be beneficial for interpreting

Table 1
IR Vibrational Band Assignments and Peak Wavenumber Positions for HC$_3$N Ice at Each Temperature Studied

Peak Position (cm^{-1})						Assignment	Assignment Reference
30 K	50 K	70 K	90 K	110 K	113 K		
88.7	...	90.1	92.9	87.4	...	Lattice[a]	2, 4
98.4	95.6	...	...	98.4	95.6	Lattice[a]	2, 4
105.3	101.1	101.1	101.1	105.3	105.3	Lattice[a]	2, 4
114.9	106.6	108.0	109.4	...	116.3	Lattice[a]	2, 4
227.6	226.3	227.6	227.6	227.6	229.0	ν_7; C≡C-C bend[a]	1, 2, 3
...	495.8	495.8	495.8	495.8	495.8	ν_6; C-C≡N bend	...
505.4	505.4	505.4	505.4	505.4	505.4	ν_6; C-C≡N bend[a]	1, 2, 3, 4, 5
693.7	675.9	671.8	680.0	675.9	675.9	ν_5; C≡C-H bend	...
755.6	758.4	757.0	755.6	754.3	754.3	ν_5; C≡C-H bend[a]	1, 2, 3, 4, 5
882.1	883.5	883.5	882.1	882.1	882.1	ν_4; C-C stretch[a]	1, 2, 3, 4, 5
996.3	997.6	996.3	994.9	994.5	993.5	$\nu_5 + \nu_7$	1
1029.3	1030.6	1030.6	1030.6	1029.3	1029.3	$2\nu_6$	1, 2, 3
...[b]	...[b]	1268.5	1269.9	...	1268.5	?	...
1368.9	1368.9	1368.9	1368.9	1370.3	1370.3	?	...
1488.5	1492.6	1491.3	1488.5	1487.1	1485.8	$2\nu_5$	1, 2, 3, 4, 5
1738.8	1738.8	1738.8	1738.8	1738.8	1738.8	$2\nu_4$ (?)	...
1884.5	1884.5	1884.5	1884.5	1884.5	1884.5	?	...
2031.6	2031.6	2031.6	2031.6	2030.3	2030.3	ν_3; C≡C stretch	4
2048.1	2046.8	2046.8	2046.8	2046.8	2046.8	ν_3; C≡C stretch	2, 4
2056.8	2056.4	2056.4	2056.4	2057.3	2057.3	ν_3; C≡C stretch	2, 4
2066.0	2066.0	2066.0	2066.0	2066.0	2066.0	ν_3; C≡C stretch[a]	1, 2, 3, 4, 5
2225.5	2224.1	2224.1	2224.1	2224.1	2224.1	C≡N stretch (**not HC$_3$N**)	...
2269.5	2270.9	2270.9	2269.5	2269.5	2269.5	ν_2; C≡N stretch[a]	1, 2, 3, 4, 5
2500.5	2504.6	2500.5	2504.6	2504.6	2504.6	$\nu_2 + \nu_7$ (?)	...
2572.0	2570.6	2570.6	2570.6	2570.6	2570.6	$\nu_3 + \nu_6$	1
2768.6	2768.6	2768.6	2768.6	2768.6	2767.3	$\nu_2 + \nu_6$	1
2940.5	2940.5	2940.5	2940.5	2940.5	2940.5	sp^3 C-H stretch (**not HC$_3$N**)	...
3018.9	3010.6	3010.6	3010.6	3010.6	2998.3	?	...
3090.4	3090.4	3090.4	3090.4	3089.0	3089.0	sp^2 C-H stretch (**not HC$_3$N**)	...
3139.9	3138.5	3138.5	3138.5	3138.5	3138.5	$\nu_2 + \nu_4$	1, 4, 5
3205.9	3201.8	3203.1	3203.1	3203.1	3204.5	ν_1; C-H stretch[a]	1, 2, 3, 4, 5
3284.3	3284.3	3285.6	3284.3	3284.3	3284.3	ν_1; C-H stretch	...
3296.6	3298.0	3299.4	3299.4	3299.4	3299.4	$\nu_2 + 2\nu_6$ (?)	...
...	3336.5	...	3336.5	3335.1	3335.1	?	...
...	3434.1	...	...	...	...	?	...
3545.0	...	...	3351.0	...	...	?[c]	...
...	3757.3	3757.3	3754.5	...	...	?	...
3958.0	3956.6	3955.3	3955.3	3955.3	3955.3	$\nu_1 + \nu_5$	5
4079.0	4076.3	4077.6	4079.0	4080.4	4080.4	$\nu_1 + \nu_4$ (?)	...
4123.0	4121.6	4121.6	4121.6	4121.6	4121.6	$2\nu_3$ (?)	...
4195.9	4194.5	4190.4	4190.4	4193.1	4189.0	?	...
4321.0	4321.0	4321.0	4321.0	4319.6	4319.6	?	...
4336.1	4336.1	4336.1	4336.1	4336.1	4336.1	?	...
4516.3	4519.0	4517.6	4519.0	4517.6	4517.6	?	...
4543.8	4538.3	4539.6	4538.3	4538.3	4538.3	$2\nu_2$ (?)	...
4678.5	4677.1	4677.1	4675.8	4674.4	4674.4	?	...
5256.0	5251.9	5253.3	5254.6	5256.0	5256.0	$\nu_1 + \nu_3$ (?)	...
5467.8	5463.6	5463.6	5465.0	5466.4	5466.4	$\nu_1 + \nu_2$ (?)	...
5535.1	5536.5	...	5536.5	5535.1	5535.1	?	...
5887.1	...[b]	5881.6	5878.9	...[b]	5883.0	?	...
6180.0	6180.0	6178.6	6178.6	6178.6	6178.6	?	...
6279.0	6279.0	6277.6	6276.3	6276.3	6274.9	$2\nu_2 + 2\nu_4$ (?)	...
6406.9	6397.3	6400.0	6402.8	6404.1	6405.5	$2\nu_1$ (?)	...
6588.4	6589.8	...	...	...	...	?	...

Notes.
[a] The median line center accuracy over temperature is ±0.72 cm^{-1} for the lattice; ±0.01 cm^{-1} for ν_1, ν_2, ν_3, and ν_6; ±0.02 cm^{-1} for ν_4 and ν_5; and ±1.03 cm^{-1} for ν_7.
[b] Peaks that are <3σ detection.
[c] Peaks that reduce in intensity and area when depositing with helium gas.

References. (1) Turrell et al. (1957); (2) Nolin et al. (1976); (3) Masterson & Khanna (1990); (4) Dello Russo & Khanna (1996); (5) Borget et al. (2001).
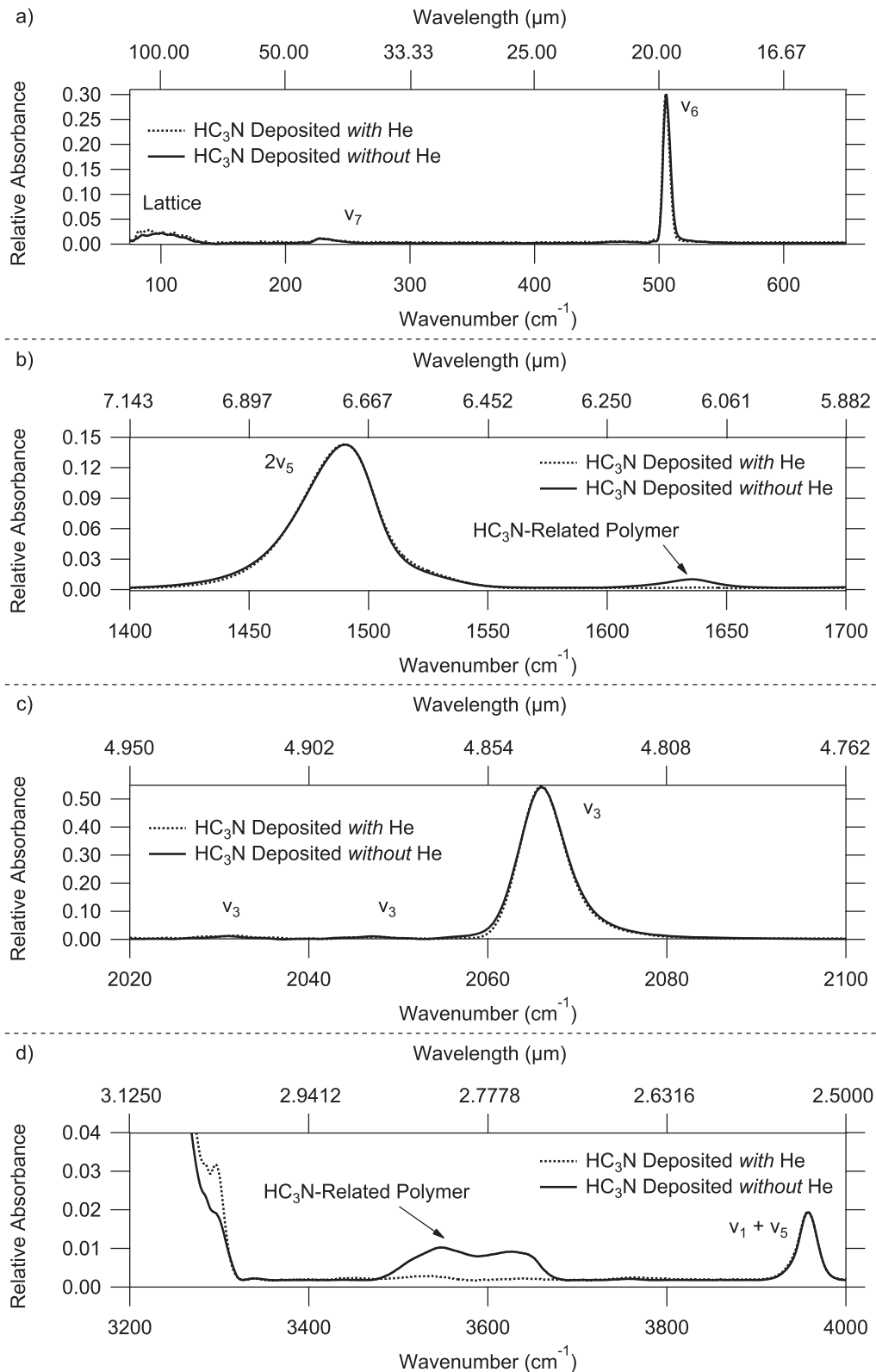
Figure 1. HC$_3$N ice absorbance spectra as functions of wavenumber from direct vapor depositions at 30 K over four different wavenumber ranges: (a) 75–650 cm^{-1} (133.3–15.4 μm), (b) 1400–1700 cm^{-1} (7.14–5.88 μm), (c) 2020–2100 cm^{-1} (4.95–4.76 μm), and (d) 3200–4000 cm^{-1} (3.125–2.500 μm). The dotted curves depict HC$_3$N ice *with* helium gas included during vapor deposition, and the solid curves show HC$_3$N ice *without* helium gas included during vapor deposition. Comparison between the two curves reveals that incorporation of helium during the HC$_3$N vapor deposition procedure greatly reduces the formation of HC$_3$N-related polymers to below the spectrometer's detection limit. This is easily observed in the ~1600–1660 cm^{-1} (~6.25–6.02 μm) and ~3500–3700 cm^{-1} (~2.86–2.70 μm) vicinities (panels b and d), while the remaining spectral dependencies of the ice features remain comparable. When formed with and without helium, the HC$_3$N ice thicknesses are 0.75 ± 0.02 and 2.60 ± 0.07 μm, respectively. For comparison purposes, the thinner HC$_3$N ice film was scaled by factors of 3.10 (panels a and d), 3.40 (panel b), and 2.55 (panel c).
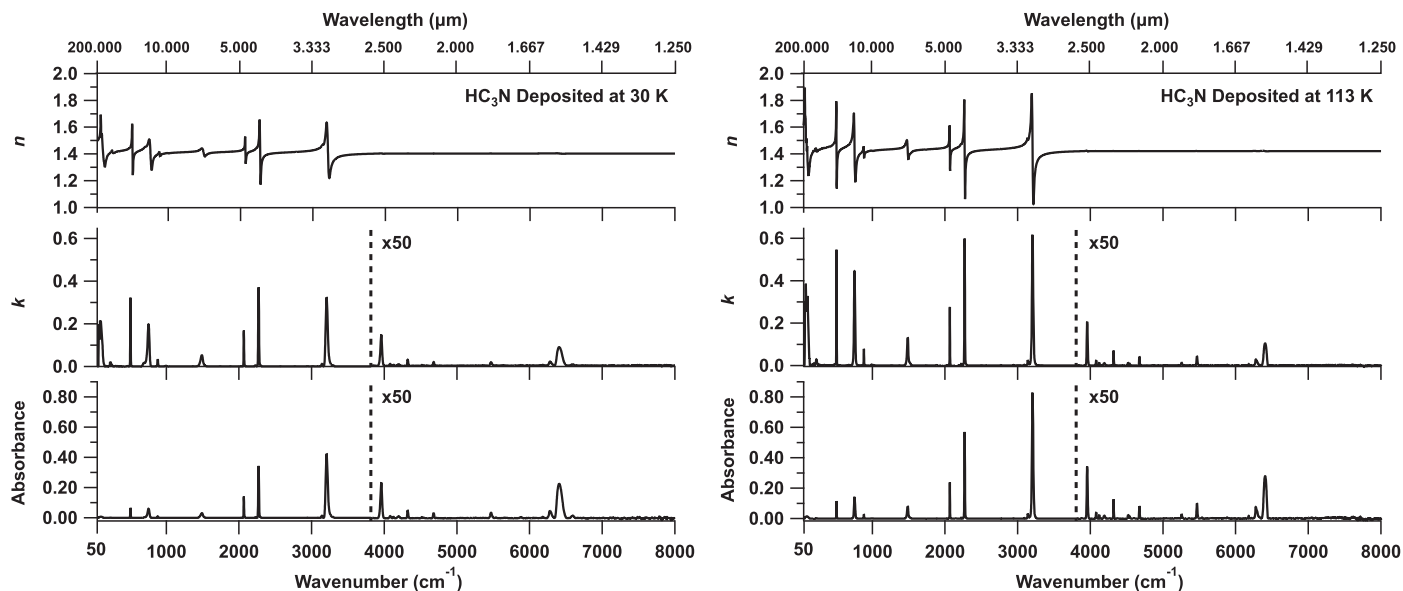
Figure 2. The spectral dependence of the HC$_3$N ice absorbances (lower panels), the imaginary part of the refractive indices (k; middle panels), and the real part of the refractive indices (n; upper panels) from 50 to 8000 cm^{-1} (200 to 1.25 μm). The left-hand side depicts amorphous HC$_3$N (vapor was deposited at 30 K) and the right-hand side shows crystalline HC$_3$N (vapor was deposited at 113 K). The absorbance features and corresponding k values at wavenumbers greater than 3800 cm^{-1} (wavelengths shorter than 2.63 μm) have been multiplied by 50 in order to assist in viewing the higher wavenumber (smaller wavelength) near-IR features of the weaker combination and overtone bands of HC$_3$N ice. Ice thicknesses are 0.75 ± 0.02 and 0.78 ± 0.02 μm for the amorphous and crystalline phases, respectively.
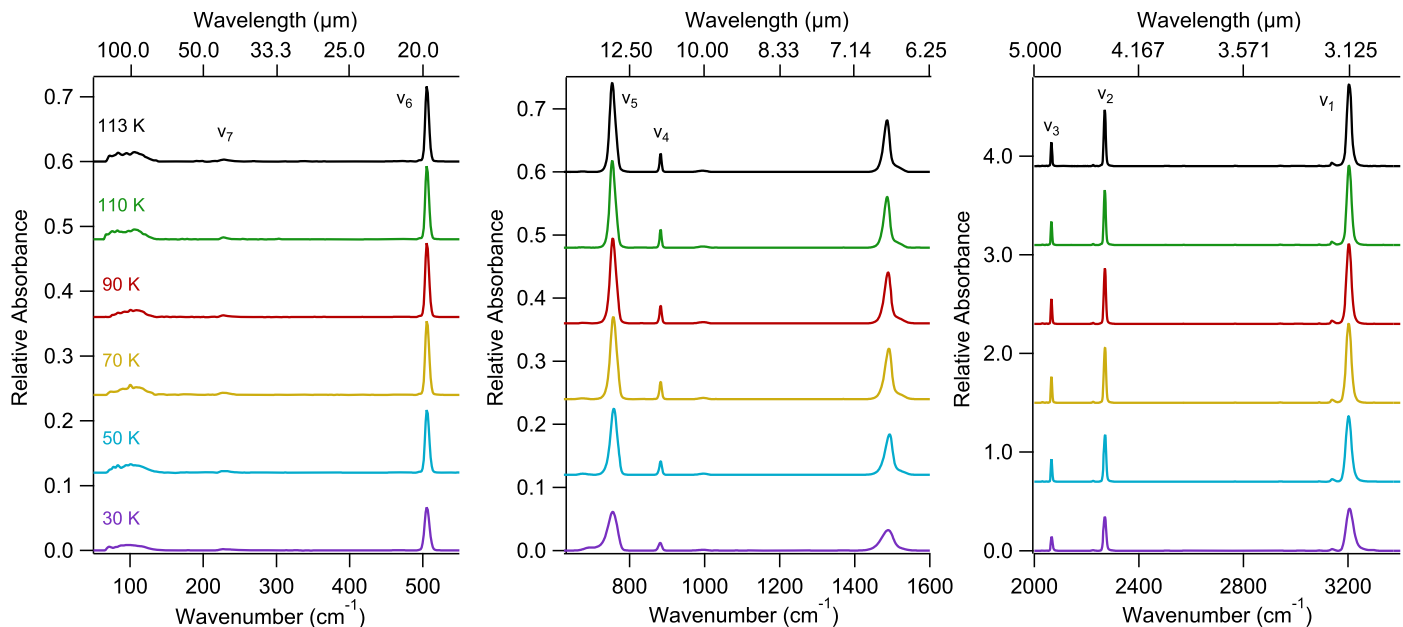
Figure 3. HC$_3$N ice absorbance spectra depicting the fundamental vibrational modes (ν_1–ν_7) at deposition temperatures 30 (purple curves), 50 (blue curves), 70 (yellow curves), 90 (red curves), 110 (green curves), and 113 K (black curves). The lattice vibrational mode near 100 cm^{-1} ($\sim$100 μm) and the $2\nu_5$ overtone near 1500 cm^{-1} ($\sim$6.67 μm) are also visible. The left and middle panel spectra are vertically offset from each other by a factor of 0.12, and the right panel spectra are vertically offset from each other by a factor of 0.7. Ice thicknesses are 0.75 ± 0.02, 0.76 ± 0.02, 0.82 ± 0.02, 0.81 ± 0.02, 0.79 ± 0.02, and 0.78 ± 0.02 μm, at 30, 50, 70, 90, 110, and 113 K, respectively.

spectra from Cassini's Visible and Infrared Mapping Spectrometer (VIMS; spectral range $\sim$1–5 μm), as well as the Near Infrared Spectrograph (NIRSpec; spectral range 0.6–5 μm) on the upcoming JWST.

We assess the crystalline temperature of an ice by monitoring the ice's absorption bands and the IR channel fringes over a 24 hr period (Anderson et al. 2018a); an ice held at its crystalline temperature will not sublime within our high vacuum chamber configuration during this time. The ice has been formed at the crystalline temperature only if there are no

observed changes in band shape, band strength, band position, and the number of IR channel fringes. Figure 5 demonstrates the spectral dependence of the amorphous to crystalline phases for HC$_3$N ice, focusing on the ν_5, ν_2, and ν_1 bands. As the ice is formed at increasingly warmer temperatures, there is a transition from disordered amorphous to partially ordered amorphous that begins at cold temperatures between 30 and 70 K, and then gradually continues until the transition to crystalline is complete by 113 K. This is evidenced by the steep narrowing of the bandwidths and the transition of a shoulder on
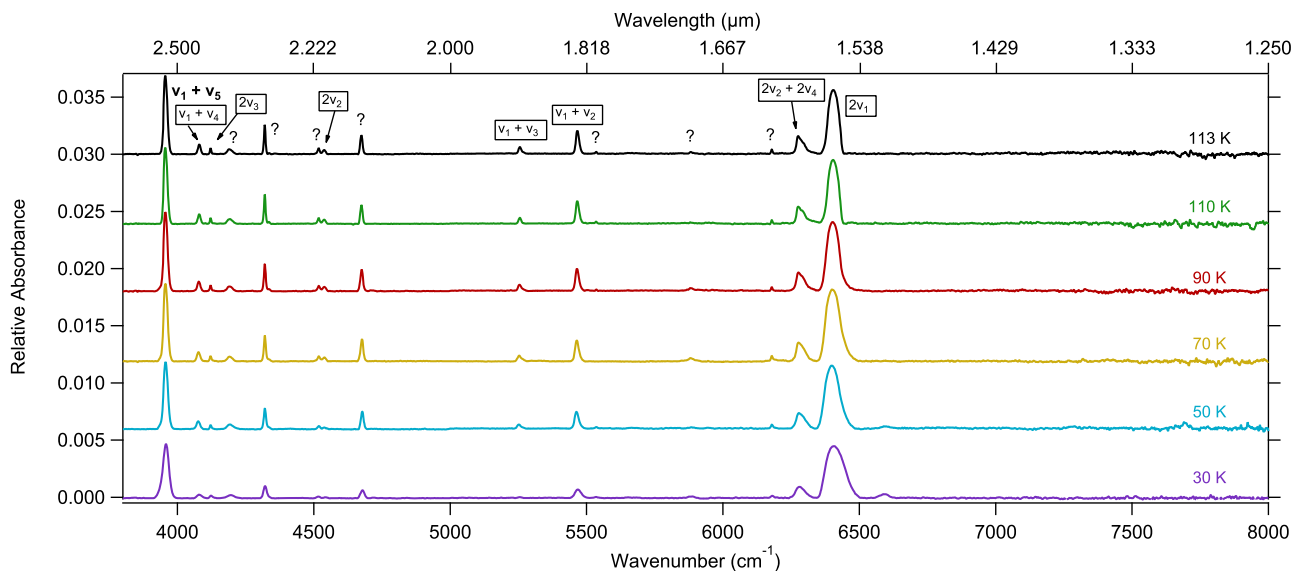
Figure 4. HC$_3$N ice absorbance spectra from 3800 to 8000 cm^{-1} (2.63 to 1.25 μm) as functions of deposition temperatures of 30 (purple curve), 50 (blue curve), 70 (yellow curve), 90 (red curve), 110 (green curve), and 113 K (black curve). The $\nu_1+\nu_5$ combination band assignment is indicated, as are the potential assignments for the $\nu_1+\nu_4$, $\nu_1+\nu_3$, $\nu_1+\nu_2$, and $2\nu_2+2\nu_4$ combination bands, as well as the $2\nu_1$, $2\nu_2$, and $2\nu_3$ overtone bands (all potential assignments are labeled in rectangles). Unassigned HC$_3$N features are denoted with a question mark. Absorbance spectra are vertically offset from each other by a factor of 0.006.
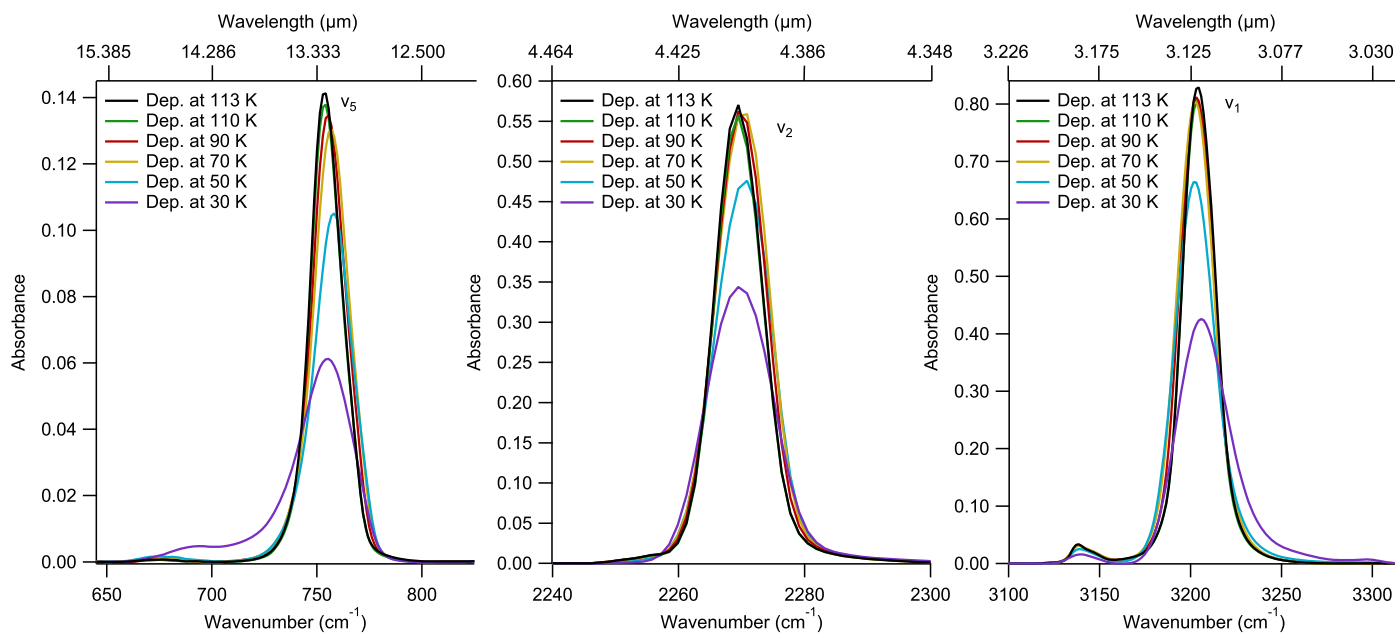
Figure 5. HC$_3$N ice absorbance spectra for the ν_5 band (left panel), the ν_2 band (middle panel), and the ν_1 band (right panel). HC$_3$N ice was formed at deposition temperatures of 30 (purple curve), 50 (blue curve), 70 (yellow curve), 90 (red curve), 110 (green curve), and 113 K (black curve). The disordered and partially ordered amorphous phases ($T < 113$ K) and the crystalline phase ($T \geqslant 113$ K) are noted by the bandwidth narrowing and peak center shifts with increasing temperature, and all spectral changes terminate once the ice is formed at or above the crystalline temperature.

the ν_5 that shifts to lower energies when the ice is formed at temperatures above 30 K. Khanna (2005) also observed a transition at low temperature from disordered amorphous to partially ordered amorphous for annealed HC$_3$N ice, and it was attributed to the simpler linear structure of HC$_3$N having no freely rotating -CH$_2$ or -CH$_3$ groups. In the present study, a complete crystalline structure was achieved at temperatures $\geqslant$113 K, with no observed spectral changes at deposition temperatures >113 K. The band shifts corresponding to the final lowest energy state of the ice (i.e., crystalline) are most noticeable for the ν_1 band peak center, eventually centering at 3204.5 cm^{-1} by 113 K.

Previous Titan-relevant nitrile studies that annealed an amorphous ice to its crystalline temperature reported a wide range of crystalline temperatures for HC$_3$N. Both Dello Russo & Khanna (1996) and Moore et al. (2010) determined the crystalline temperature of HC$_3$N ice under their respective experimental conditions to be 110 K. On the other hand, Masterson & Khanna (1990) determined the crystalline temperature of HC$_3$N ice to be 90 K, and Khanna (2005) alluded to the HC$_3$N crystalline temperature being between 100 and 120 K. While these publications do not discuss the reasons for the crystalline temperature variations, they may be related to differences in experimental methodologies (i.e., annealing to
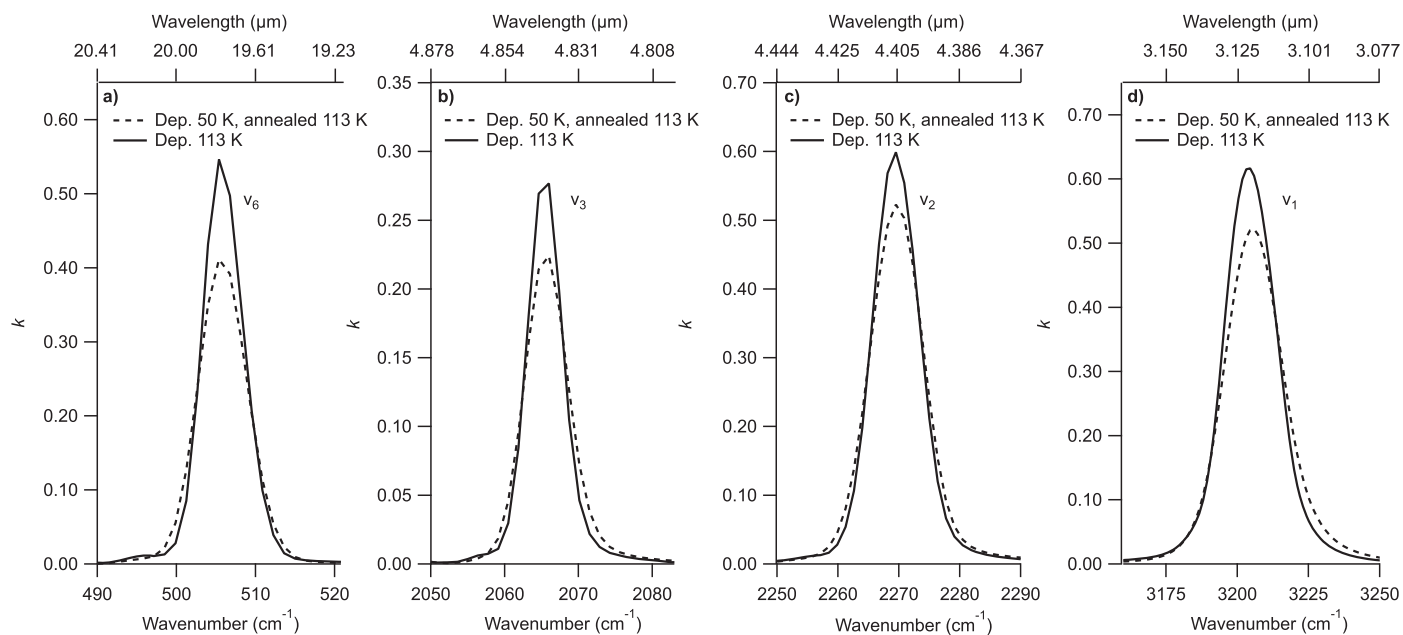
Figure 6. The imaginary part of the refractive index (k) for the ν_6 (panel a), the ν_3 (panel b), the ν_2 (panel c), and the ν_1 (panel d) fundamentals of HC_3N ice. Solid curves depict HC_3N vapor deposition directly into its crystalline phase at 113 K. Dashed curves illustrate HC_3N vapor deposition at 50 K (amorphous phase) that is then annealed to its crystalline temperature of 113 K, following the procedures described in Dello Russo & Khanna (1996) and Moore et al. (2010). These four fundamental modes reveal differences in their spectral dependencies due to the ice formation method employed (directly deposited or annealed).

find the lowest energy state of the ice) and vapor deposition techniques/flow rates used to make the thin ice films.

Based on the altitudes where HC_3N ice has been observed in Titan's stratosphere (see Coustenis et al. 1999; Anderson & Samuelson 2011; Anderson et al. 2018b), HC_3N ice is expected to form directly at (or very close to) its crystalline temperature. Therefore, having optical constants of HC_3N ice formed directly at this temperature is crucial, since an ice annealed from the amorphous phase to its crystalline temperature will never fully convert to crystalline (Sandford & Allamandola 1990; Moore et al. 2010; Anderson et al. 2018a, 2018b; Nna-Mvondo et al. 2019). Figure 6 demonstrates that there are spectral differences (and therefore structural differences) between an ice that was formed by vapor deposition directly into the crystalline phase at 113 K (solid line) and an ice that was annealed to 113 K, following vapor deposition into the amorphous phase at 50 K (dashed line). For the annealing experiment, the methods described in Dello Russo & Khanna (1996) and Moore et al. (2010) were followed, where the ice was held at the crystalline temperature for 65 minutes for the far-IR measurements, and 120 minutes for the mid-IR measurements. While some of the differences between the two ices' spectral dependencies are subtle, the peak centers of the annealed ice are shifted, most apparent with the ν_1 band (which shifted 1.4 cm^{-1} toward higher energy), and have different line widths when compared to the ice formed directly into its crystalline phase at 113 K.

The conclusions found by Sandford & Allamandola (1990), Moore et al. (2010), and Nna-Mvondo et al. (2019) that an ice annealed to the crystalline temperature reaches a unique, less-ordered lowest energy state compared to that of an ice formed directly at the crystalline temperature (or warmer), is reflected in our studies with HC_3N ice as well. This possibly explains why different studies in the literature report a range of

crystalline temperatures since annealing is not able to reach the full crystalline phase, but its own lowest (noncrystalline) energy state at a given temperature. To further demonstrate that annealing cannot reach the same ordered state as an ice formed directly into the crystalline phase, we performed annealing experiments where HC_3N ice was held at the crystalline temperature for longer amounts of time (up to 92 hr) and at temperatures warmer than the 113 K crystalline temperature (annealed from 50 to 120 K and 30 to 130 K). In all of these experiments, the identical result was met where the annealed ice each time achieved the same less-ordered lowest energy state, which differed compared to when HC_3N ice formed directly into the crystalline phase. We assessed this by comparing the spectral dependencies of the three annealed ices to that of the ice formed directly into the crystalline phase.

The bulk structural differences of an ice annealed to the crystalline temperature compared to an ice formed by directly depositing the vapor at its crystalline temperature reinforces the need for HC_3N optical constants at direct vapor deposition temperatures. These optical constants are greatly needed to more accurately simulate environments and analyze remote sensing data where HC_3N ice forms directly from vapor condensation processes. Even though the differences in peak wavenumber positions and line widths appear small for HC_3N ice, these subtle spectral variations will still affect cloud retrievals, where the width of the line determines the mean particle radius and the line strength determines the particle abundance. This is also especially important to consider for Titan's stratosphere where this experimental data can help determine if observed ice spectral features correspond to the pure compounds or those compounds when in mixtures, without adding the uncertainty of using the spectral dependence of an annealed ice in the analysis (e.g., Anderson & Samuelson 2011; Anderson et al. 2018a, 2018b).

4. Summary

Absorbance spectra of HC_3N ice formed at 30, 50, 70, 90, 110, and 113 K were measured from 50 to 8000 cm^{-1} (200 to 1.25 μm), and the corresponding optical constants for these ices were calculated for the first time. Numerous unassigned combination and overtone bands have now been given assignments. Additionally, comparing the spectral dependence of annealed versus direct deposited HC_3N ice at 113 K further demonstrates that annealing does not fully convert an amorphous ice into the crystalline phase. Therefore, additional direct deposit experiments specifically performed at Titan-relevant stratospheric temperatures for all organic compounds expected to condense in Titan's stratosphere are greatly needed. By performing transmission IR spectroscopy on HC_3N ice formed at direct vapor deposition temperatures instead of by annealing, we are now providing optical constants for HC_3N ice that was formed in a way that mimics HC_3N ice cloud formation in Titan's stratosphere. The HC_3N optical constants at each vapor deposition temperature will be available on the PDS Atmospheres Node at New Mexico State University and also on the Spectroscopy for Planetary ICes Environments (SPICE) laboratory website: https://science.gsfc.nasa.gov/693/spicelab/.

ORCID iDs

Melissa S. Ugelow https://orcid.org/0000-0001-9725-6624
Carrie M. Anderson https://orcid.org/0000-0003-2175-3709

References

Anderson, C. M., Nna-Mvondo, D., Samuelson, R. E., McLain, J. L., & Dworkin, J. P. 2018a, ApJ, 865, 62
Anderson, C. M., & Samuelson, R. E. 2011, Icar, 212, 762
Anderson, C. M., Samuelson, R. E., Achterberg, R. K., Barnes, J. W., & Flasar, F. M. 2014, Icar, 243, 129
Anderson, C. M., Samuelson, R. E., Bjoraker, G. L., & Achterberg, R. K. 2010, Icar, 207, 914
Anderson, C. M., Samuelson, R. E., & Nna-Mvondo, D. 2018b, SSRv, 214, 125
Anderson, C. M., Samuelson, R. E., Yung, Y. L., & McLain, J. L. 2016, GeoRL, 43, 3088
Bockelée-Morvan, D., Lis, D. C., Wink, J. E., et al. 2000, A&A, 353, 1101
Borget, F., Chiavassa, T., Allouche, A., Marinelli, F., & Aycard, J.-P. 2001, J. Am. Chem. Soc., 123, 10668
Chapillon, E., Dutrey, A., Guilloteau, S., et al. 2012, ApJ, 756, 58
Coates, A. J., Wellbrock, A., Lewis, G. R., et al. 2009, P&SS, 57, 1866
Condon, J. J. 1997, PASP, 109, 166
Coustenis, A., Schmitt, B., Khanna, R. K., & Trotta, F. 1999, P&SS, 47, 1305
de Bergh, C., Schmitt, B., Moroz, L., Quirico, E., & Cruikshank, D. 2008, in in The Solar System Beyond Neptune, ed. M. A. Barucci (Tucson, AZ: Univ. Arizona Press), 483
Dello Russo, N., & Khanna, R. K. 1996, Icar, 123, 366
Domingo, M., Millán, C., Satorre, M., & Cantó, J. 2007, Proc. SPIE, 6616, 66164A
Ferris, J., Sanchez, R., & Orgel, L. 1968, J. Mol. Biol., 33, 693
Frere, C., Raulin, F., Israel, G., & Cabane, M. 1990, AdSpR, 10, 159
Gladstone, G. R., & Young, L. A. 2019, AREPS, 47, 119
Graupner, M., Field, T., Youngs, T., & Marr, P. 2006, NJPh, 8, 117
Hörst, S. M. 2017, JGRE, 122, 432
Khanna, R. K. 2005, Icar, 178, 165
Khanna, R. K., Perera-Jarmer, M. A., & Ospina, M. J. 1987, AcSpA, 43, 421
Kunde, V. G., Aikin, A. C., Hanel, R. A., et al. 1981, Natur, 292, 686
Lavvas, P., Lellouch, E., Strobel, D. F., et al. 2020, NatAs, 5, 289
Lellouch, E., Gurwell, M., Butler, B., et al. 2017, Icar, 286, 289
Maguire, W. C., Hanel, R. A., Jennings, D. E., Kunde, V. G., & Samuelson, R. E. 1981, Natur, 292, 683
Masterson, C. M., & Khanna, R. K. 1990, Icar, 83, 83
Miller, F., & Lemmon, D. 1967, AcSpA, 23A, 1415
Moore, M. H., Ferrante, R. F., Moore, W. J., & Hudson, R. 2010, ApJS, 191, 96
Moureu, C., & Bongrand, J. 1920, Ann. Chim, 14, 47
Nna-Mvondo, D., Anderson, C. M., & Samuelson, R. E. 2019, Icar, 333, 183
Nolin, C., Weber, J., & Savoie, R. 1976, JRSp, 5, 21
Orgel, L. E. 2002, OLEB, 32, 279
Patel, B. H., Percivalle, C., Ritson, D. J., Duffy, C. D., & Sutherland, J. D. 2015, NatCh, 7, 301
Powner, M. W., Gerland, B., & Sutherland, J. D. 2009, Natur, 459, 239
Quirico, E., Douté, S., Schmitt, B., et al. 1999, Icar, 139, 159
Raulin, F., & Owen, T. 2002, SSRv, 104, 377
Sagan, C., & Thompson, W. R. 1984, Icar, 59, 133
Samuelson, R. E. 1985, in ESA Special Publication, Vol. 241, The Atmospheres of Saturn and Titan (Paris: ESA), 99
Samuelson, R. E. 1992, in ESA Special Publication, Vol. 338, Symp. on Titan (Paris: ESA), 191
Samuelson, R. E., Mayo, L. A., Knuckles, M. A., & Khanna, R. J. 1997, P&SS, 45, 941
Samuelson, R. E., Smith, M. D., Achterberg, R. K., & Pearl, J. C. 2007, Icar, 189, 63
Sandford, S. A., & Allamandola, L. J. 1990, ApJ, 355, 357
Tempelmeyer, K. E., & Mills, D. W., J. 1968, JAP, 39, 2968
Turner, B. E. 1971, ApJ, 163, L35
Turrell, G. C., Jones, W. D., & Maki, A. 1957, J. ChPh, 26, 1544
Vinatier, S., Schmitt, B., Bézard, B., et al. 2018, Icar, 310, 89
Wong, M., Fan, S., Gao, P., et al. 2017, Icar, 287, 110
Yung, Y. L., Allen, M., & Pinto, J. P. 1984, ApJS, 55, 465